Precision X-Ray Spectroscopy of 3C 273 Jet Knots

by

Mark J. Avara

Submitted to the Department of Physics
in partial fulfillment of the requirements for the degree of

Bachelor of Science

at the

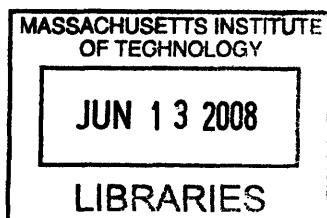MASSACHUSETTS INSTITUTE OF TECHNOLOGY

June 2008

© Massachusetts Institute of Technology 2008. All rights reserved.

Author . . . . . . ,
Department of Physics
May 20, 2008

Certified by . . . .
Dr. Herman L. Marshall
Principal Research Scientist, MKI
Thesis Supervisor

Certified by . . . .
Dr. Jacqueline N. Hewitt
Professor of Physics; Director, MKI
Thesis Reader

Accepted by . . .

Professor David E. Pritchard
Senior Thesis Coordinator, Department of Physics

Precision X-Ray Spectroscopy of 3C 273 Jet Knots

by

Mark J. Avara

Submitted to the Department of Physics
on May 20, 2008, in partial fulfillment of the
requirements for the degree of
Bachelor of Science

Abstract

We present results from precision X-ray spectroscopy using high-resolution ($\Delta\lambda = 0.01$Å) spectra of 3C 273 jet knots extracted from eight observations made using Chandra in conjunction with the HETGS. Using these spectra we searched for narrow emission line candidates and, based on significance values calculated for the observed photon counts in each bin of the spectrum of the entire jet, we selected three possible emission candidates and attempted to match these with known highly emissive X-ray emission lines. From this calculation we found the temperature of the X-ray emitting plasma to be $10^{6.8}$ K, the bulk velocity of the knots to be 0.78 times the speed of light, and the electron density in the jet to be $0.043\pm^{.007}_{.009}$cm^{-3}.

Thesis Supervisor: Dr. Herman L. Marshall
Title: Principal Research Scientist, MKI

Acknowledgments

Contents

List of Figures

List of Tables

Chapter 1

Introduction

1.1   History of X-ray Astrophysics

We have come a long way from the first known human-made observatory possibly built 7000 years ago near present day Gosek, Germany, to the modern era of high-energy astronomy. Though, the human interest in high-energy astronomical events must go back to the dawn of man when a strange powerful light might have brightened a moon-less night. This was once the only evidence we had for extra-solar high-energy astrophysical events.

We are now searching for understanding of these highest energy astrophysical objects, many of which still partially or fully elude us. In this thesis I describe our findings from the search for narrow emission lines in the X-ray spectrum of the jet in the AGN 3C 273, and explain why the search for a more complete understanding of Active Galactic Nuclei (AGN) is an important part of modern astrophysics.

Some of the highest energy phenomena in the Universe are far away and otherwise faint and in order to learn details about the nature of the universe and the physical processes therein we need ways to peer farther into the sky than the eye allows and to make observations in all regions of the electromagnetic spectrum. The development of different fields of physics has historically defined the limits of astronomical observation, and the 20th century, the so called "Golden Age" of physics, has allowed astounding leaps forward in astronomical observation and thus the development of

astrophysics, cosmology, and our entire understanding of the universe. The development of Quantum Mechanics, Einstein's Special and General theories of relativity, the Standard Model of particle physics, and the new questions which will feed research into the next century have had astounding impacts on the range of processes in the universe we can observe and have pushed for new developments to broaden it further. The study of astrophysical objects which emit X-rays and even higher electromagnetic energy in the form of gamma rays, in association with the development of particle physics, has lead to a new frontier in physics, particle astrophysics. The research in this field pushes our understanding of the highest energy mechanisms in the known universe. The focus of this paper, X-ray astrophysics involving outflows of particles from high energy extra-galactic objects called AGN, is actively being incorporated into this new field and some physicists believe some of the highest energy particles we detect, cosmic rays, may come from jets of AGN.

1.2 A New Opportunity With 3C 273

Quasars, point-like sources often similar to typical spiral galaxies [19] like our own in size but sometimes much more luminous at their center, were first discovered during the first radio surveys of the sky in the late 1950's. By that point in time the angular resolution of radio telescopes was precise enough in order to identify the strongest radio sources with individual optical objects. Many of these were galaxies, but a few were stellar-like sources.

One of the most important of these radio surveys was that of the 3C, or third Cambridge, catalog (Edge et al. 1959). This survey involved observations made at 158 MHz, and its revision, the 3CR catalog (Bennett 1961), at 178MHz. These surveys detected sources with limiting fluxes down to 9 Jy[1]. There are 471 3C sources numbered by right ascension. 3C 273 has epoch 1950.0 (this is just a reference date for which coordinates of objects have a particular set of values.) coordinates $\alpha_{1950} =$

---

[1]A jansky (Jy) is a unit of specific flux, defined as 1 Jy $= 10^{-26}$ watts m^{-2} Hz^{-1} $= 10^{23}$ ergs s^{-1} cm^{-2} Hz^{-1}.

$12^h26^m33^s.35$, $\delta_{1950} = +02^o19'42''$. All sources in the 3C catalog are north of -22° declination.

Photometry of these confusing stellar-like sources with spectra showing broad emission lines generally not found in stellar spectra revealed they are anomalously blue relative to normal stars. 3C 273 was found to be star-like by an accurate lunar occultation measurement (Hazard, Mackey, and Shimmins 1963), and the first real understanding brought to this new phenomena was the discovery by Maarten Schmidt (Schmidt 1963) that the emission lines seen in 3C 273's spectrum were hydrogen Balmer-series emission lines and Mg II $\lambda2798$ at the surprisingly large redshift of z=0.158. At the time, this was among the very most highly redshifted objects known, approximately an order of magnitude larger than those of the first Seyfert galaxies, rivaled only by a few very faint galaxy clusters. The distance to 3C 273 can be found by the interpretation of the redshift to be of cosmological origin, a consequence of the expansion of the Universe [19]:

$$d = cz/H_0 = 3000zh_0^{-1} \text{ Mpc} \tag{1.1}$$

where h_0 is the Hubble constant in units of 100 km / s / Mpc. 3C 273 is about 100 times as luminous as other spiral galaxies such as the Milky Way and remains the brightest known source of its kind. Once the mystery of the spectrum, namely being highly redshifted, was unlocked, identification of emission lines in other quasar spectra followed. These became known as 'quasi-stellar radio sources', which was subsequently shortened to 'quasars'.

The important of quasars is signified in their extremely high luminosities. These luminosities suggest that supermassive black holes of even ~ 1 million to ~ 1 billion solar masses might be present, the role of active nuclei in galaxy formation and evolution was considered, and such high luminosity objects can be used as possible probes for studying cosmology and the structure of the universe since they can be detected at extraordinary distances. These were all strong motivations for continued searches for and identification of quasars. More details about the physics of quasars

and quasar jets will be discussed in Chapter 2.

In 1987 Harris & Stern detected X-ray emission from the jet of 3C 273 using data from the Einstein Observatory. They found the jet to have a flux in X-rays of less than 1% of the flux of the core. Observations with the ROSAT HRI with resolution $\sim$ 15" resolved the individual knots of the jet (Roser et al. 2000), but it is Chandra's unprecedented look into the X-ray universe which has allowed for a detailed study of X-ray emitting jets in quasars not previously possible and the detection of X-ray emitting jets beyond those in the nearest and brightest active galaxies (Marshall et. al 2004). This has brought about a new era in the study of extragalactic jets (a recent review is given by Harris & Krawczynski 2006). With eight observations of 3C 273 and its jet totaling 234 ks of exposure, we now have the opportunity to study the high-resolution X-ray spectrum of the jet in 3C 273 with enough collected photons to search for bright X-ray emission lines. We present the results of this study.

1.3 Chandra

The Advanced X-ray Astrophysics Facility (AXAF), renamed Chandra X-Ray Observatory (CXO) in honor of the famous astrophysicist Chandrasekhar after being successfully launched on July 23, 1999, combines a highly efficient high-resolution ($\leq$ .5 arcsec) X-ray telescope with a suite of advanced imaging and spectroscopic instruments [6]. Chandra's Internal Propulsion System placed it in a high elliptical orbit where it carries out its mission as the X-Ray component of NASA's four Great Observatories: Chandra, the Hubble Space Telescope, the late Compton Gamma-Ray Observatory, and the Spitzer Space Telescope. Chandra, shown diagrammatically in Figure 1-1, was designed to provide order-of-magnitude advances in spatial and spectral resolution over previous X-ray missions. Images with half-power diameter (HPD) of the point spread function (PSF) of less than 0.5 arcsec are taken with the High Resolution Mirror Assembly (HRMA). The two gratings, the High Energy Transmission Grating (HETG) and the Low Energy Transmission Grating (LETG), proved resolving powers ($\lambda/\Delta\lambda$) well over 500 over much of their bandwidth, which together
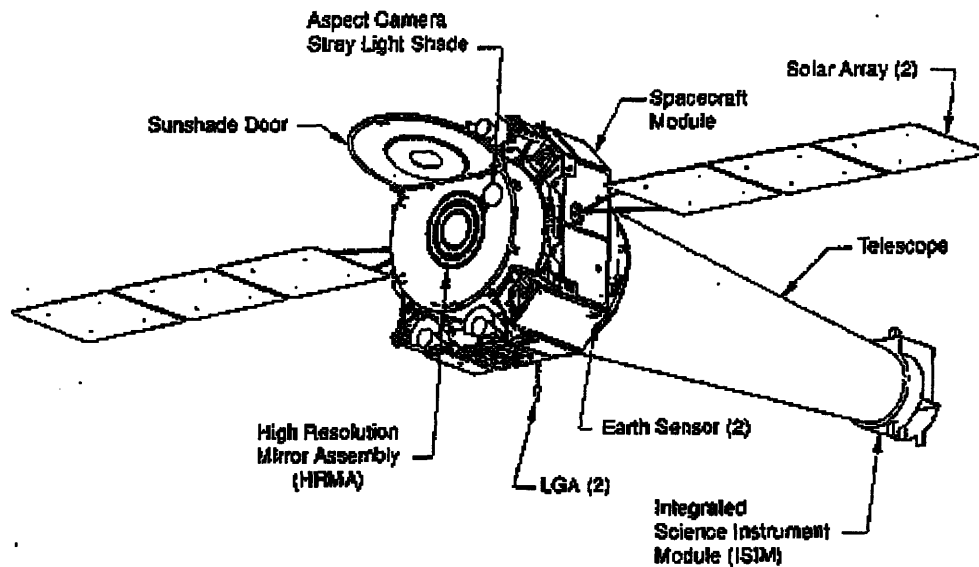
Figure 1-1: Diagram of the primary instruments and modules of the Chandra X-ray Observatory. [6]

covers approximately the range 0.1 to 10 keV.

The HRMA consists of four nested paraboloid-hyperboloid (Wolter type-1) grazing incidence X-ray mirror pairs with a focal length of 10 m and a largest diameter of 1.2 m. These focus images onto the focal-plane scientific instruments (SIs) which are staged on the Science Instrument Module (SIM), which consists of hardware providing mechanical and thermal interfaces for the SIs. Arranged on the SIM in the focal plane are the imaging instruments, of which I have been concerned with the ACIS-S imaging array of charged coupled devices (CCDs).

1.3.1 ACIS

The two focal instruments, the Advanced CCD Imaging Spectrometer (ACIS) and the High Resolution Camera (HRC) are each comprised of two principal components. ACIS-I is a 4-chip CCD array designed for CCD imaging and spectrometry. ACIS-S is a 6-chip CCD array, all in line, which can be used for CCD imaging spectrometry and for high-resolution spectroscopy in conjunction with the HETG grating. ACIS-S has four front illuminated and two back-illuminated CCDs, one of which is at the

best focus position for the HRMA. Each CCD is flat but they are mounted in order to better align on the focal plane.

1.3.2 HETG

The Instrument Principal Investigator for the HETG is Prof. Claude Canizares, of the MIT Kavli Institute for Astrophysics and Space research. When operated with the ACIS-S it forms the High Energy Transmission Grating Spectrometer (HETGS) for high resolution spectroscopy in the band between 0.4 and 10.0 keV. The HETGS achieves resolving power ($E/\Delta E$) as high as 1000 in this band. The HETG is comprised of two grating assemblies, the High Energy Grating (HEG) and the Medium Energy Grating (MEG). These are held on a module, as seen in Figure 1-1, which can be placed on command in the optical path just behind the HRMA. The MEG is in the optical path of the outer two shells of the HRMA and the HEG is in the path of the inner two, and the dispersion directions of these two gratings have a 10 degree separation so they can be distinguished. The diffraction gratings disperse into several orders according to the diffraction equation given in Chapter 5. The 0th order image is nearly that of the image as it would be without the gratings. The second and third orders are dispersed onto the length of the ACIS-S instrument. A comparison between the effective areas of the grating spectrometers is shown in Figure 1-2.
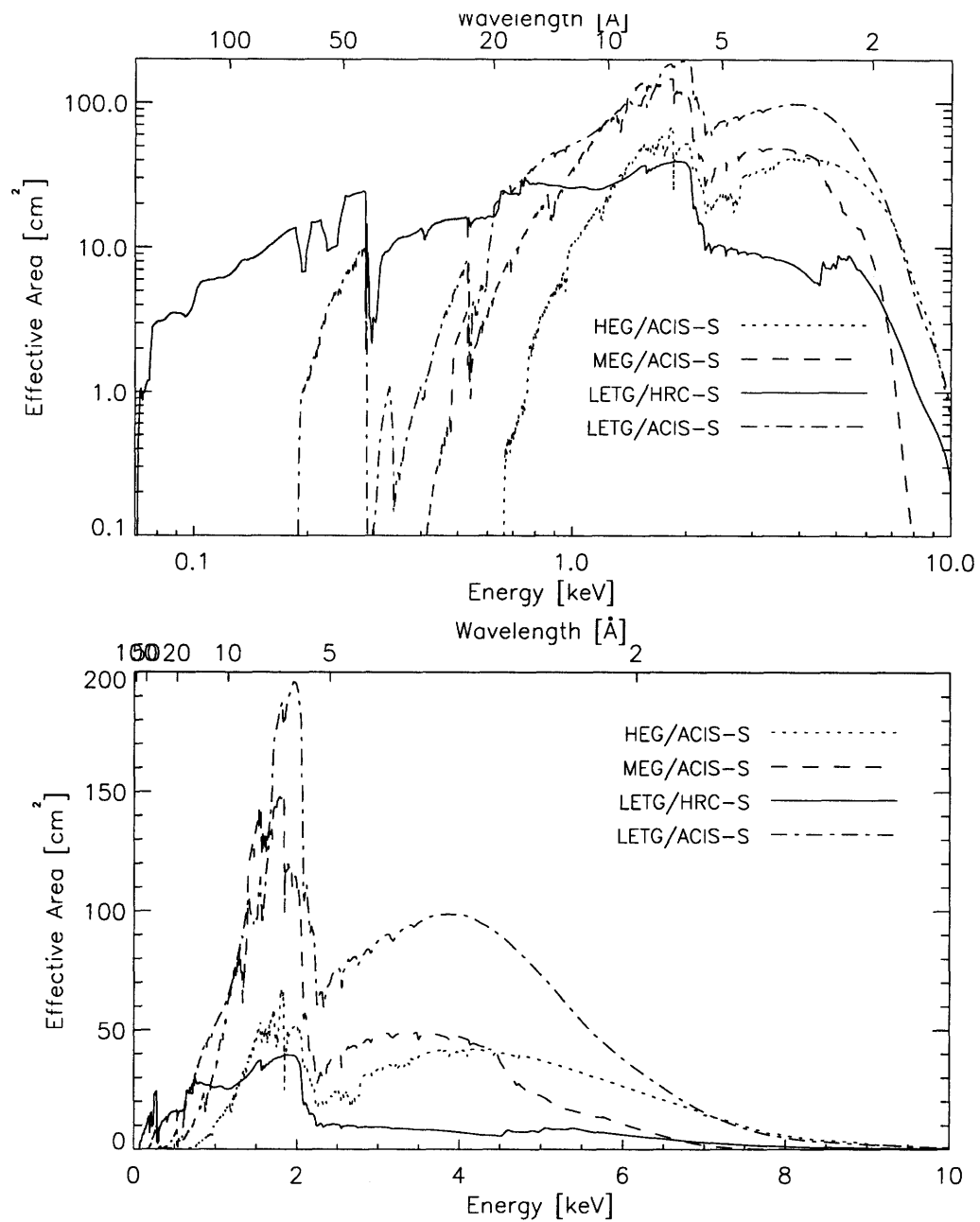
Figure 1-2: Comparison of the first order effective areas integrated over the line spread function. Both the +1 and -1 orders, the dispersion in either direction for the gratings, have been included. [6]

19

Chapter 2

Quasars and Jets

In this chapter I go into some of the detail of theoretical and observational work that has been done in the search for understanding of the class of astrophysical objects that 3C 273 falls under.

2.1 AGN

The term 'active galactic nucleus', or AGN, refers to the existence of energetic phenomena in the central regions, or nuclei, of galaxies which is not clearly a result of emission from stars. [19] The two primary subclasses of AGN are Seyfert galaxies and quasars. The fundamental difference between them is the ratio of total amount of radiation emitted by the compact core to that emitted by all the stars of the galaxy. The core of a typical Seyfert galaxy emits about the same amount of radiation as the stars, $\sim 10^{11} L_\odot$, where $L_\odot$ is the luminosity of the Sun, but the typical luminosity of the nucleus of a quasar is 100 or more times that of the stars.

Woltjer (1959) was the first to make a clear attempt to understand the physics of Seyfert galaxies. He noted that: 1) the nuclei are unresolved, which implies the size of the nucleus must be less than 100 parsecs (pc), 2) the nuclear emission must last more than 10^8 years (the result of several simple arguments based on the fact that about 1 in 100 spiral galaxies are Seyfert galaxies), and 3) if the nuclear material is gravitationally bound, the nuclear mass must be very high. This last result is from

the simple virial argument

$$M \approx \frac{v^2 r}{G}. \qquad (2.1)$$

The velocity dispersion can be found by measuring the widths of emission lines (i.e. Doppler broadening) and is on the order of $10^3 \mathrm{km\ s}^{-1}$. A lower limit can be placed on r to be greater than $\sim 1\mathrm{pc}$ from typical plasma densities for plasmas which emit the observed spectral lines, and an upper bound on r comes from 1). Therefore, the mass of the nucleus can be inferred to be in the range $M \approx 10^{9 \pm 1}\ M_\odot$. This suggests that about 10% of the mass of a Seyfert galaxy is contained in the central region with diameter about 100pc. This is strong evidence for supermassive black holes lying at the center of many galaxies.

X-ray observations are important for gaining understanding of AGN. X-rays account for $\sim 10\%$ of the bolometric luminosity of AGN and often have rapid variability which indicates X-rays provide a probe of the innermost regions of AGN where the scale of high energy phenomena is small enough to change quickly.

By 1964, Schmidt had studied a sufficient number of quasars to define the following properties (Schmidt 1969): star-like objects identified with radio sources, time-variable continuum flux, large UV flux, broad emission lines, and large redshifts. However, not all AGN have all these properties. A modern unifying characteristic is their broad spectral energy distributions (SEDs). In general the broad-band SED of the continuum of the spectra of quasars can be described by a power law [19].

2.2   The Jet Phenomenon

Two other subclasses of AGN, and the difference between all four classes is blurred to some degree, are radio galaxies and blazars. In the early days of radio astronomy the second discrete source of strong radio waves other than the Sun was found in the constellation Cygnus and was named Cygnus A [5]. Using accurate positioning of the radio source by F. Graham Smith, Baade & Minkowski were able to find the optical counterpart, which turned out to be a peculiarly shaped galaxy. Modern radio observations of the sky have told us that this galaxy, at 240 Mpc from the Milky Way,

is the brightest radio source besides the Sun and Cassiopeia A, a nearby supernova remnant. This implies that the source must have an extremely large radio luminosity. This is one typical example of a radio galaxy. Modern imaging shows us that most of these radio galaxies have two large radio lobes, in the case of Cyg A each spanning a diameter of about $17h^{-1}$kpc, with a distance of about $50h^{-1}$kpc between the two lobes. Further observation in the radio shows a jet from the center of the galaxy spanning this distance to the nearest lobe, and a weak counter jet. This jet is typical of radio galaxies and similar collimated jets have been found in a number of AGN in the X-ray band in a recent Chandra survey (Marshall et al. 2004; Gelbord 2004). There have been no X-ray lobes found on the size scale of the radio lobes, but there are distinct knots in the X-ray images of many of these jets, including 3C 273.

Observations of superluminal velocities in jets very close to AGN core imply highly relativistic motion of the material of these jets, and many current models of the X-ray continuum emission depend on relativistic motion for efficient radiation from synchrotron processes or scattering of photons either from the plasma of the jet or from the Cosmic Microwave Background (CMB) (Jester et al. 2006), but the speed distribution of material along the length of these jets is still in debate. Detection of narrow emission lines in the X-ray spectrum of the jet knots would allow for calculation of the speed of the jet material in a new way.

The simplest source for huge outflows of energy in a small area as is evident in the luminosity of AGN, is accretion of matter onto a strong gravitational source, such as a supermassive black hole. There is strong observation evidence that jets are somehow a result of this process. Jets are seen in many accreting systems including binary systems in which matter from a donor star is falling onto a neutron star or black hole, in the formation of stars, in the centers supernova remnants, as well as galactic AGN. Most of the models for creation of these outflows depend on the environment of the accretion disk and there is little if any evidence of jets existing in non-accreting systems. One of the primary models involves large magnetic fields in the plasma of the accretion disk acting to both accelerate and collimate the charged particles of the plasma into a narrow bipolar jet. This process occurs at the energy expense of the

accreting material.

Chapter 3

Spectral Analysis of 3C 273's Jet

We acquired eight observations of 3C 273, imaging both core and jet, by the Chandra X-Ray telescope since its launch. These observations, summarized in Table 3.1, totaling 236.58 ks exposure time, have primarily been used for ongoing effective area calibration, and were all taken with the HETG grating placed in the light path with photons collected by the ACIS-S instrument.

The archived data was received with preliminary processing done by Chandra's on-board computers and ground processing before archiving for scientific use. The ground processing produces a FITS file containing a list of photon events from the ACIS-S CCD's. Our data reduction starts with the events list. Figure 3-1 shows the image from the FITS event list for ObsID 2463 of 3C 273.

Table 3.1: Chandra Observations of 3C 273

Observation ID	Start Date	Exposure (ks)
459	2000-01-10	39.06
2463	2001-06-13	27.13
3456	2002-06-05	25.00
3457	2002-06-05	25.38
3573	2002-06-06	30.16
4430	2003-07-07	27.60
5169	2004-06-30	30.17
8375	2007-06-25	30.04
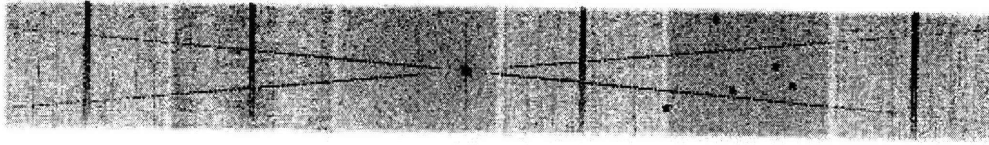
Figure 3-1: Photon events from the ACIS-S CCD array in conjunction with the HETG when observing 3C 273 during Chandra calibration observation number 2463. The core of 3C 273 is the bright dot located in the third CCD. Separation between CCDs shows up as faint vertical streaks. Dark vertical streaks are due to bad CCD columns and there is a faint streak from the core extending vertically due to CCD readout. The two diagonal lines are the HEG and MEG spectra.

3.1 Overview

I wrote analysis software in the Interactive Data Language (IDL) image processing language, building on analysis scripts written for general processing of spectra from both the HEG and MEG gratings of the HETG. Adjusted versions of these scripts were used for standard steps in processing the data and new code was written in order to combine the photon events in the dispersed spectra from all eight observations.

The processing of the events files produced spectra in the form of photon count as a function of wavelength for background and source selection regions. Each observation was handled separately and the final spectra were combined for fitting to a model. Deviations from the power law model represent either emission or absorption lines, or deviations in the continuum model for the general radiative processes in the jet.

3.2 Preliminary Processing

The events list was first filtered for streaks, which are columns of pixels whose data are effected by pileup, or 'over exposure' for the CCD. Parameters such as the exposure time were estimated or read in from the FITS events list and header files where possible. The events were shifted so that the zeroth order image center was located on knot A. The shift direction for each observation was determined by taking the bin with maximum counts in a histogram of counts at each angle around the annulus with minimum and maximum radial bounds of (0., 50) pixels containing knots A, B,

and C. The knots of the x-ray jet provide separation between luminous regions and are summarized in Figure 3-2. This is accurate enough for our purposes since the distribution of the jet in X-rays along position angle -138.°0 is 0."33 ± 0."01 (full width at half max of 0."78) according to Marshall et al. (2001), and the ACIS pixel size is 0.4920±0.0001 arcsec. The shift along the jet profile in order to center knot A for spectral analysis was estimated based on the histogram of counts along the profile of the jet to be between 25.6 and 26.0 pixels, which is between 12.6 and 12.8 arcsec on the sky, in agreement with Marshall et al. (2006) to within 1.9 percent. This accuracy is less important since I later shift each event in the entire dispersed spectra (all orders) for core and jet so that the dispersed spectral images of the jet knots will be aligned in the cross-dispersion direction for identical wavelength. This is important when preparing spectra from the images for the x-ray emission of the entire jet so that possible narrow emission lines and other features will not be spread out in wavelength space by the shape of the jet. This tilt can be seen in Figure 3-3.

The event coordinates r_i, where r_r is the coordinate of right ascension and r_d is that of declination, were then transformed from sky coordinates to angular coordinates of projection by the mirrors according to the equation:

$$\theta_i = \frac{(r_i - r_i^{knotA})\text{FS}}{\text{R}} \qquad (3.1)$$

where the Rowland Spacing R = 8.63265 m is the diameter of the Rowland torus on which each grating's center is placed (Born and Wolf, 1980; Canizares et al., 2005 the HETG design fabrication) and the focal length F = 10.061620 m is the focal length of the HRMA. θ_i is the deflected angle from the mirror. The sky scale is 0.0001366667° and is a conversion factor between degrees on the sky and pixels on the CCDs.

We then rotated the array of events in sky coordinates by the roll angle of the telescope for each observation and by the angle of the HEG and MEG dispersion directions with respect to the y axis of the ACIS-S CCD array (y axis is along the length of the six CCDs). Thus, the two event arrays prepared for the HEG and MEG spectra are (θ_d, θ_x), the angles along the dispersion direction of each grating, θ_d, and
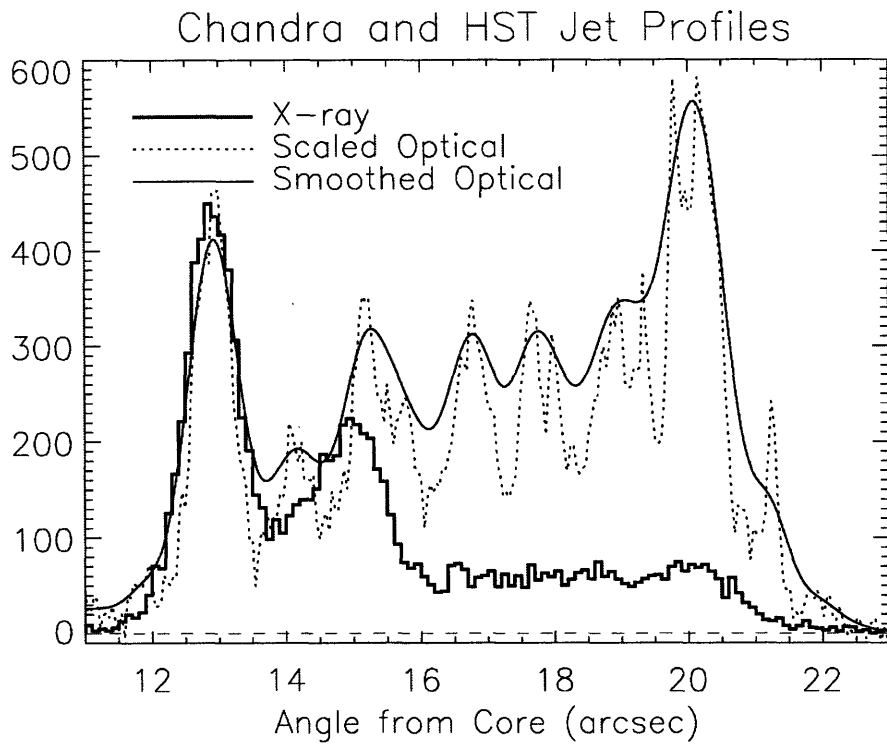
Figure 3-2: Counts along the profile of the jet in optical and X-ray bands. In the X-ray band, the first peak is distinguished as Knot A and the the section between 14" to 16" is Knot B. (Figure from [16])
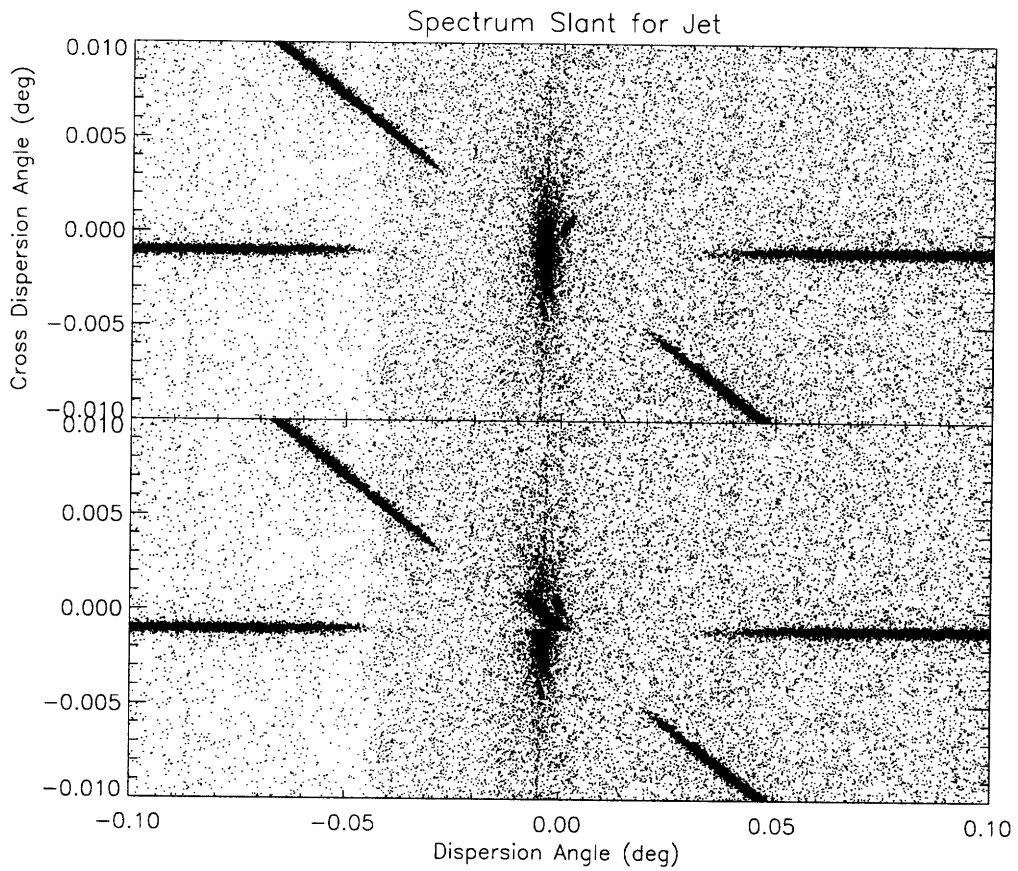
Figure 3-3: Cleaned dispersed spectral images on the CCD's before and after the slanting transformation used to align the spectral bins of the knots.

cross dispersion direction, θ_x, for each event. Directly after this stage of processing, the slice along the dispersed direction which contains the jet was tilted in order to align the knots in the cross dispersion direction, as mentioned before.

We determined the diffraction order, m, for each event by comparing $m\lambda$, which is also equal to dispersion angle times the grating period, $d\theta_d$, to the energies of the photons as measured by the ACIS CCDs. This relation is the diffraction grating equation in the small angle approximation, $\sin(\theta) \simeq \theta$.

$$d(\sin \theta_{\mathrm{d}}(\lambda) - \sin \theta_{\mathrm{i}}) = \mathrm{m}\lambda \tag{3.2}$$

is the full grating equation, which simplifies to

$$d(\theta_{\mathrm{d}}(\lambda) - \theta_{\mathrm{i}}) = \mathrm{m}\lambda \tag{3.3}$$

in this approximation. d is the spacing between the grating slits, and θ_i is the angle of the incident photon. We compare the λ from this equation to the wavelength derived from the energy E from the CCD using the standard equations

$$E = h\nu \tag{3.4}$$

$$c = \nu\lambda \tag{3.5}$$

$$E = \frac{hc}{\lambda} \tag{3.6}$$

where $h = 6.626 \times 10^{-27}$ erg s is Planck's constant and $c = 2.998 \times 10^{10}$ cm s^{-1} is the speed of light.

We remove distortions in the image due to bright or otherwise bad pixels after pulse height filtering in order to reduce the impact of certain columns which primarily effect low energy pulse heights. By this stage of processing we have data ready to be binned into spectra.

3.3 Creation of Spectra and Spectral Model

In this section, unless otherwise specified, all techniques were applied for the events in both the HEG and MEG transforms of the original events list.

Continuing the theme of using values of $m\lambda$ for each event, an array of the values $|(E/hc)*m\lambda|$ was made, where E is the CCD energy of the event. Since E/hc is equivalent to $1/\lambda$ (a rearrangement of 3.4) this expression is a calculation of the order of diffraction for each X-ray photon event. These values are used to discern events in each order and include them in the spectra appropriately. Note that these values of E for each photon event were adjusted by a gain value specific to each of the four nodes on all six CCD chips. All gain values were small, [0.95, 1.0] times the CCD energy, and were found by manually adjusting these values until the m for photons averaged over each chip node separately appeared to align with each other at m=1.

An array of values, either 0 or 1 for false and true, was then calculated from an expression testing several conditions. Either

1. m > .88 and

2. m < 1.12 and

3. $|m\lambda| > 6.$ Å

or

1. m > 0 and

2. $|m\lambda| < 6.$ Åand

3. $|m - (\text{target order})| < .02 * |m\lambda|$ (target order is the order of the selection the test is for)

Two sets of rules are used for the regimes in which $m\lambda < 6.0$ and $m\lambda > 6.0$ because in the first of these two limits .88 and 1.12 gives too large a range for dependable selection of photons not due to noise. Thus, a linear scaling with the small values of $m\lambda$ is used. These values, however, are unique to the boundary conditions for the

31

Table 3.2: Test Expressions for Order Selection

Events Selection	Target Order	m_{min}	m_{max}	Test for $m\lambda$	$m\lambda$ Coefficient
HEG Plus	1	.88	1.12	> 6.	
	1			< 6.	.02
HEG Minus	1	.85	1.15	< -5.	
	1			> -5.	-.03
MEG Plus	1	.75	1.25	> 10.	
	1			< 10.	.025
MEG Minus	1	.85	1.15	< -6.	
	1			> -6.	-.025

HEG first order dispersion events on the plus side of the dispersion direction (defined to be positive values of m). Table 3.2 lists the selection values for both MEG and HEG for first and second order dispersed events. Note that blank spaces indicate lack of corresponding test. These boundaries are designed to allow for some discrepancy in wavelength as calculated from CCD energies and dispersion distance, but to eliminate background by only selecting those photons for which these match to a high degree.

The last step in selection of good photon events was to combine and apply these filters. This was done by creating new arrays for both MEG and HEG events containing the time of selected events, the cross dispersion angle in degrees, the dispersion order (based on tests listed above, specified as strictly ±1 or ±2), and mλ. The filters for this selection of events were those for bad columns due to bright or otherwise bad pixels, the tests for energy matching given above, a selection of only events with $|\theta_x| < 0.°01$, and that for streaks in the first stages of our processing.

In order to maximize the extraction of useful spectral information from these eight observations careful attention was placed on selecting the largest X-ray background and spectrum source regions possible. Figure 3-4 shows our selection regions for the dispersed HEG spectrum of the jet in ObsID 2463 of 3C 273.

For each knot selection for each observation spectra of three regions were created by histograming the values of mλ divided by the order of the event, for all events, for each order in each dispersion direction. The source selection region, containing the spectrum of the jet knots of interest, was specified by the cross-dispersion swath
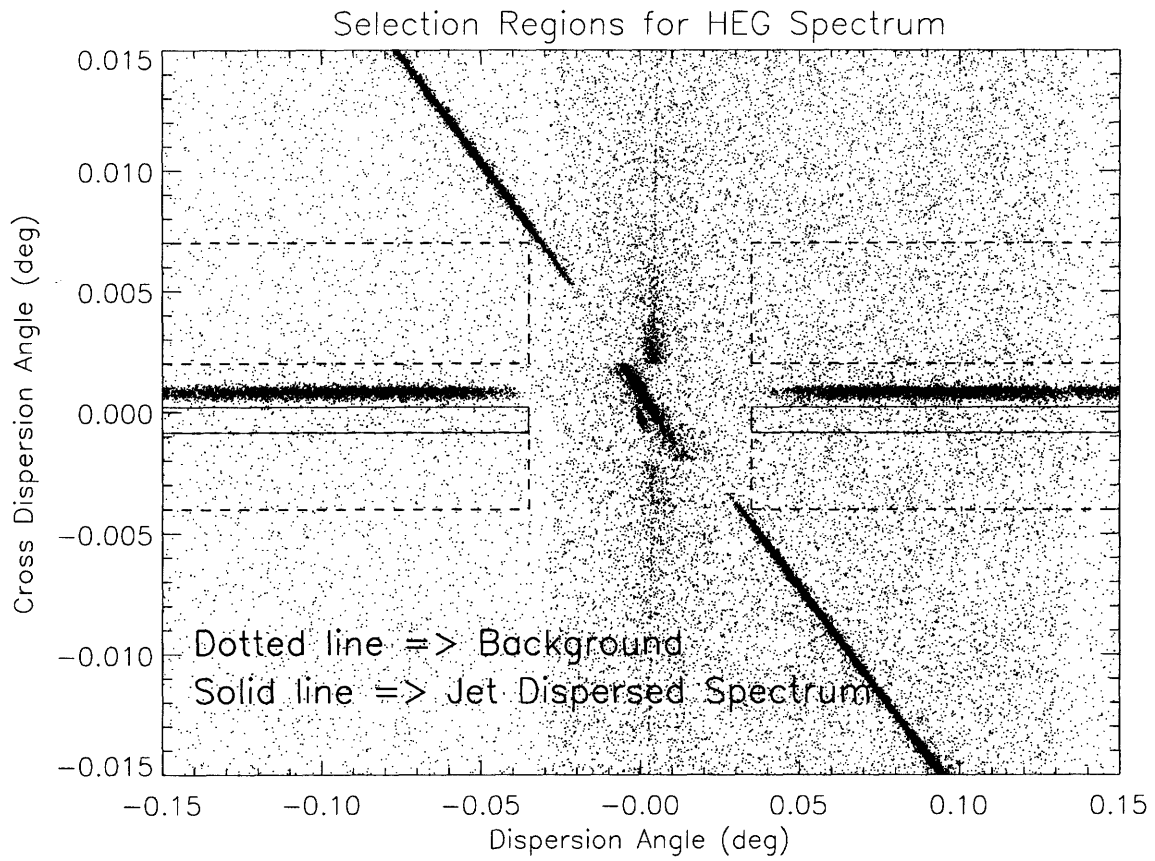
Figure 3-4: Selection regions for background and source of the HEG dispersion for ObsID 2463.
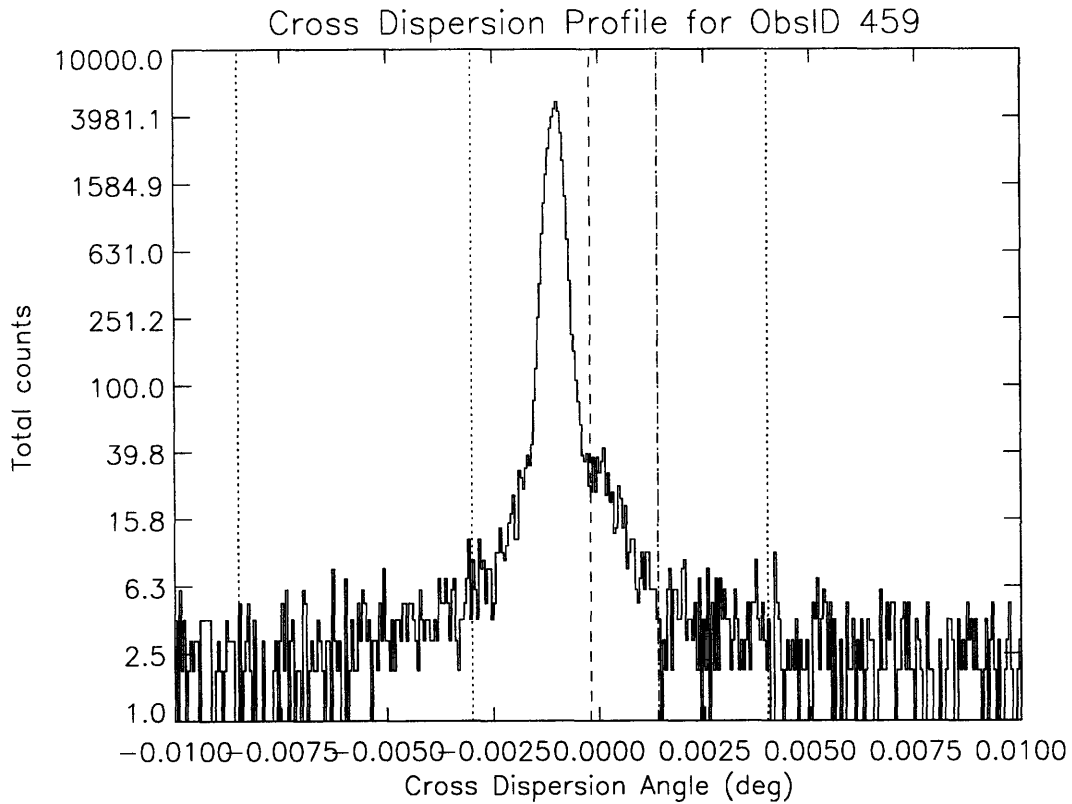
Figure 3-5: Profile of the core and jet of 3C 273 in counts as a function of cross dispersion angle. The background and source selection regions are bounded by dotted lines and dashed lines respectively.

of the knots. The background regions were specified in order to contain all photons alongside the jet dispersion for as large a region as possible and still exclude photons from the other dispersion grating or the core of 3C 273. One region was taken on the side of the dispersion of the core, from the end of the X-ray jet. The other was taken on the other side of the core dispersion, starting at a distance away from the core equal to that of knot A. The purpose here was to account for background photons in the jet dispersion selection region from the bright core. Figure 3-5 shows the selection regions in the profile of the dispersed spectrum and illustrates how scattered core photons contribute to the background of the jet.

The histograms of the source and background regions are made with bins in the

34

wavelength axis of 0.005 angstroms for HEG and 0.010 angstroms for MEG, with minimum value of 1 Å. and maximums of 25. Å for HEG and 50. Å for MEG. The background ratio is a ratio of the area of the source region and the combined area of the two background regions. For all eight observations, with a source region including the entire X-ray jet, the value of the background ratio, r, was about .15. Of course, when the source region contained only a single knot this ratio becomes even smaller. This ratio is used to multiply the summed histograms of photon counts of both background regions in order to produce the background spectrum expected in the source region. The uncertainty in the counts for each wavelength bin of the spectra was determined according to Poisson statistics, to be the square root of the number of photon counts from the source spectrum, N_i, summed with the number of counts in the background regions, V_i after being scaled by the background ratio.

$$\sigma_i = \sqrt{N_i + rV_i} \qquad (3.7)$$

Note, however, that this scaling occurs before the summation of the backgrounds of all eight observations. During that summation, each observation's source and background spectra are scaled by the observation length. Subtraction of the normalized background summed spectra from the source spectra provided the net spectrum.

In order to calculate a model for the jet spectra, the effective areas of the instruments were needed. The script *tg_effarea_exposure.pro* was used to read this data from calibration files. A combination of calibration files for the ACIS quantum efficiencies, the OBF (Optical Blocking Filter) model, the HRMA effective area, MEG and HEG efficiencies, and contamination on the ACIS filter. Also in the script the wavelength boundaries for the MEG and HEG spectra are set. Photons in the region of and around these boundaries are thrown out. Finally the script *add2spec.pro* was used to finalize the spectral arrays, correct for pileup (though the jet has such small flux there is no pileup in the photon events by this stage of processing), and create the ARF for each spectrum based on the total exposure time, the chip, the effective area, and the ACIS quantum efficiencies. The ARF is a measure of the effective area,

A_{eff}, of the entire telescope (for these observations with the HETG in use) at a given wavelength in a unit time interval and has units cm^2 s. Thus, to calculate flux in a given wavelength interval one uses the equation

$$f_c = \frac{C_{src} - C_{bkg}}{A_{eff}\Delta\lambda} \tag{3.8}$$

where f_c is the spectral intensity in photons/cm^2/s/Å C_{src} is the total number of counts in wavelength bin $\Delta\lambda$, and C_{bkg} is the number of background counts for this interval.

The calculation of photon flux just described is necessary to fit a power law curve to the SED (Spectral Energy Distribution) of the jet knots in the 0.5 - 10. keV range. Especially with this small number of counts (as evident in Figure 4-1 in the next chapter) it is important to fit the SED of the *combined* MEG and HEG counts. Recall that the MEG and HEG spectra are represented by a two dimensional space of photon counts vs. wavelength. This is equivalent to photon counts vs. energy through Eqn. 3.4. Recall also that the wavelengths for each each bin containing events in the MEG spectra run from 1 to 50 Å in 0.01 Å increments and that the HEG spectra run from 1 to 25 Å with 0.005 Å increments. These spectra were combined by adding the three bins, one from MEG and two from HEG, in each 0.01 Å interval for all bins in the range 1 to 25 Å and using the MEG events for the range 25 to 50 Å where there is no contribution from the HEG. A single ARF array was also calculated from the HEG and MEG ARFs by the same procedure with a single adjustment: in the 1 to 25 Å range the average of the ARF values for the two HEG bins was added to the single MEG ARF to create the ARF for each final wavelength bin. Finally, the quantity f_c was calculated for the combined data and the wavelength axes was transformed into energies to create the full SED measured using the HETG.

With the final versions of the SED, spectra, and ARFs made for the selected knots in all eight observations, the data was combined using *jet_add_fit_vars_<knot selection>.idl*. The respective background and source spectra and ARFs for the MEG and HEG plus and minus dispersions were added together in count space. The errors

were added using quadrature and scaling to account for the different total exposure times of the observations.

The *adapt_smooth.pro* procedure was used to smooth the SEDs. The snr_target values were 20 for the MEG and 30 for the HEG SED. This smoothed summed SED is shown with residuals to a power law fit in Figure 3-6. A selection of the data points was taken for fitting. Included values were those where the ratio of flux to error in flux was greater than 2.0, and the tails were thrown out where outside the range 0.8 to 7.0 ÅÅ linear fit was made to the ln-ln plot of the SED using IDL's linfit function, but with the flux values divided by a normalization factor in order to account for absorption by the ISM (Inter Stellar Medium) along the line of sight to the jet. This normalization value is calculated using the *ism_tb.pro* procedure, which uses an interpolation algorithm to find the characteristic transmission expected at a given energy and the column density along the line of sight to 3C 273, which was taken to be $1.2*10^{20}$cm^{-2}.

The model for the spectrum (in photon counts as a function of wavelength) was calculated in a series of steps, duplicated for the MEG and HEG spectra. First, the HEG spectrum was rebinned by a factor of 2 so that each new bin of size 0.01 Å contained the total of the counts in the two parent bins. This step allows for easier statistical analysis of the combined HEG and MEG spectra. The net number of counts was found by adding the counts in each wavelength bin of the plus and minus source dispersions and subtracting the counts from the plus and minus background dispersions. A total ARF was calculated by adding the plus and minus dispersion ARFs and setting the value to 0.001 cm^2 for wavelength bins in which the value was smaller than this. IDL's *smooth.pro* procedure can be used to smooth the total net counts but best results were found without smoothing for photon counts as small as available here. A model of the SED was found using

$$F_{model} = nE^{-\gamma}A \qquad (3.9)$$

where F$_{model}$ is the photon flux expected from a simple power law emission spectrum
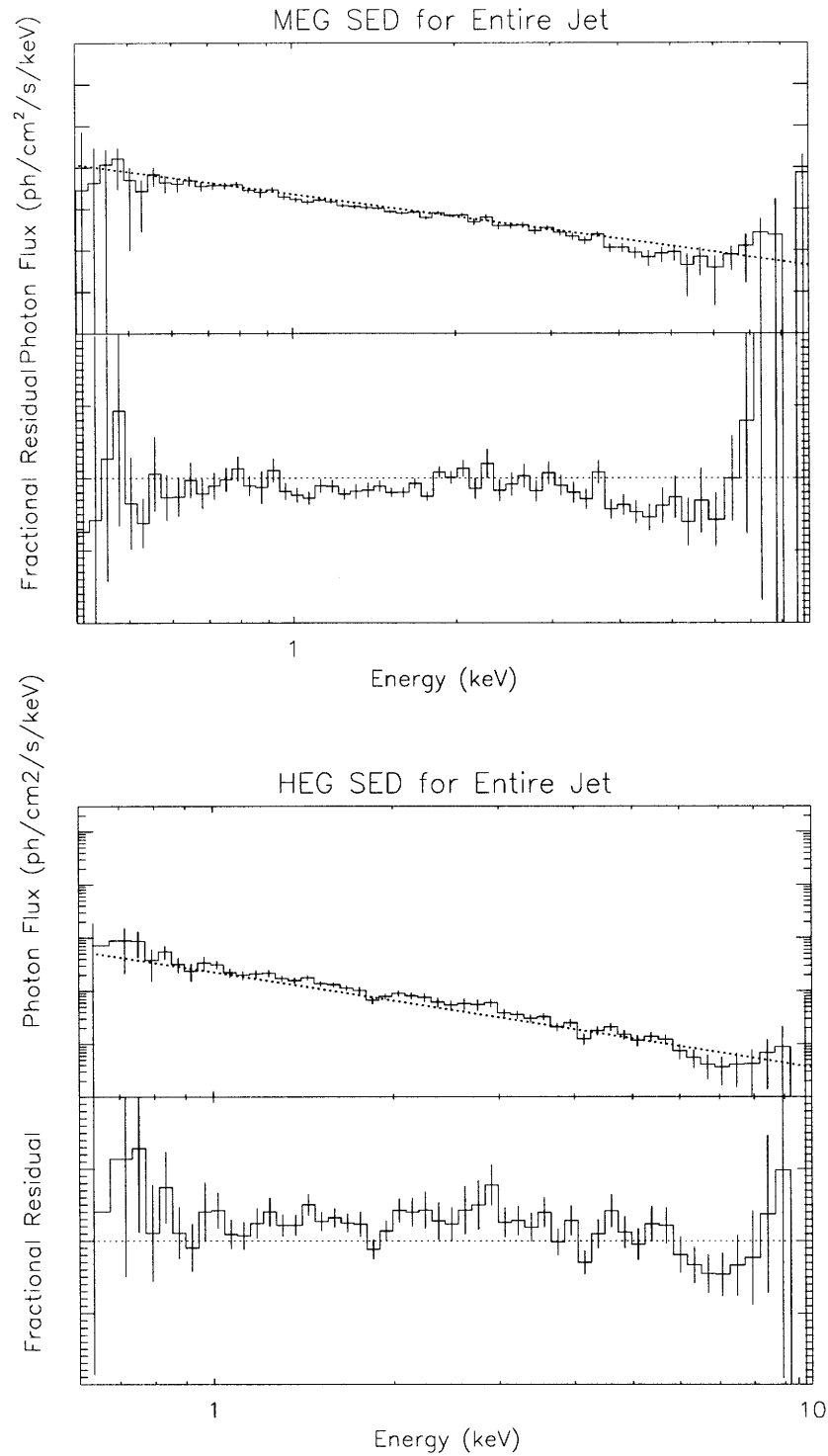
Figure 3-6: Spectral Energy Distribution of the MEG and HEG spectra of the entire jet. The log-log values, as plotted, are fit with a linear fit and the fractional residuals found by dividing the flux by the fit are shown. Note that the data is adaptively smoothed which results in unequal bin sizes.

where n is the normalization value of the SED fit, γ is the slope of the SED fit, E is the photon energy, and A is a normalization coefficient that takes into account attenuation of the signal from the jet knot due to ISM absorption. To calculate the model in strict terms of counts per wavelength bin:

$$C_{model} = F_{model} \frac{\Delta\lambda(ARF)hc}{\lambda^2} \tag{3.10}$$

Figure 4-1 shows the combined counts for both MEG and HEG compared to the model expected values. We assume simple power law emission, most likely due to synchrotron scattering in the jet, with possible narrow X-ray emission lines on top of this model. Narrow emission lines would show up as a deviation of the observed spectrum from the power law model at the wavelength of the emission line. Chapter 4 describes statistical analysis of observed deviations of photon counts from the model.

Chapter 4

Statistical Analysis

4.1 Counting Statistics

Photons arriving at the focal plane of a telescope, in this case, the array of CCD's, are considered a Poisson process. Photons satisfy the two fundamental requirements defining a Poisson process: 1) each photon arrival is in no way dependent on information about the previous photons, and 2) photons arrive at a given constant rate (time averaged over a length of time long comparable to CCD processes and the average time separation between arrivals - this process can be governed by Poisson statistics if flux from the target changes slowly). The Poisson distribution is a discrete probability distribution which gives the probability P of k events arriving in time t when the rate of arrival is r.

$$P(k;\lambda) = \frac{\lambda^k e^{-\lambda}}{k!} \tag{4.1}$$

where λ is the expected number of Poisson distributed events, in this case photon arrivals. In the statistical analysis of the high-resolution X-ray spectra of 3C 273 jet knots the statistical significance of the number of photons k_i received in a particular wavelength bin $\Delta\lambda_i$, with a model of combined power law emission and background in $\Delta\lambda_i$ of α_i, is given by the cumulative probability of receiving k_i photons or more. The probability of k_i photon events in $\Delta\lambda$ in the total exposure time of all eight

41

observations, is given by

$$S_i = \sum_{j=k_i}^{\infty} \frac{\alpha_i^j e^{-\alpha_i}}{j!}$$ (4.2)

One should note, however, that this gives the likelihood of occurrence of an emission line in $\Delta\lambda$ and to find the likelihood of occurrence of an absorption line one should instead consider the cumulative probability of receiving k_i photons or less. In these eight observations there is not a large enough total exposure time to collect enough x-ray photons in order to achieve statistical significance for narrow absorption lines so we consider here only those cases of positive fluctuation from the model.

4.2   Narrow Emission Line Candidates

Using the methods described in the previous section S was calculated for all wavelength bins between 2 and 17 Å. As is evident in 3-6, there are too few counts outside this region to trust the fit, and thus the model, and too few in order to trust calculations of significance levels of possible emission line candidates. Values of S for all bins in this range were calculated for $\Delta\lambda = 0.01$, 0.02, 0.04, 0.08, 0.16, and 0.32 Å. The finest binned data, before re-binning of the combined spectra, is that of the first bin size. In order to rebin the data, the total number of photons from the source, those expected from the model, and the background by itself contained in each pair of adjacent bins were summed. The average of their wavelengths was taken to be the central wavelength of the bin containing the combined data. At 0.32 Åbinning the bin becomes too large to effectively show the location of narrow emission lines, and broad emission lines would likely have been seen in previous observations made without the HETG, using the CCD energies to produce the spectra (Jester et al. 2006). In order to test for narrow emission lines at each of these values for $\Delta\lambda$ the data was rebinned by summing the source and background counts and averaging the effective areas for each pair of adjacent bins in order to double the bin width. There are two choices for the initial set of adjacent bin pairs for this rebinning process with resulting bin centers offset by .01 Åfrom each other. Since there is not a 100 percent correlation
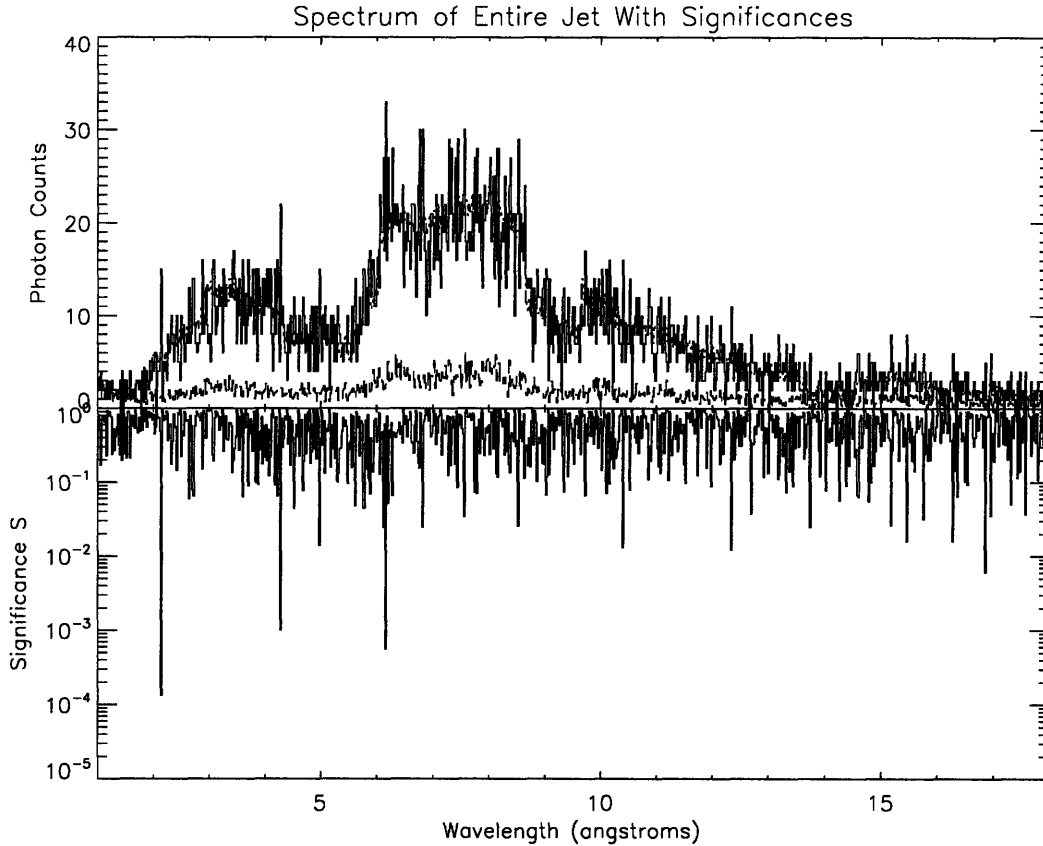
Figure 4-1: The upper plot shows the counts collected as a function of wavelength with the source plus background as a solid line, model based on background and SED fit as a dash-dot-dot line, and the background normalized to the source selection region size as a long-dash line. The lower plot gives the respective cumulative probabilities for each wavelength bin. $\Delta\lambda = .02$ since this is the second binning, and this is with initials pairs set 2.

with significance levels in 0.02 Åor larger $\Delta\lambda$ between these choices, spectra from both initial choices were considered.

Figure ?? shows the the second binning of the spectrum of the entire jet with values of cumulative probability for each bin. The process just described was used to find the significance levels of emission line candidates for three spectra: knot A, knot B plus the remainder of the jet, and the entire jet.

We then selected the wavelengths of the bins for which there were the highest significance (lowest cumulative probability) values. Table 4.1 lists the candidates in

the $2 - 17$Å range with a cumulative probability of $10^{-2.5}$ or lower and which spectrum and initial pairs selection they occur in. Note that for features at higher binnings which contain a feature at a fine binning within their $\Delta\lambda$, I list their wavelength in parentheses. Set 1 of bin pairs is the set with pairs (2.005, 2.015), (2.025, 2.035), etc. and set 2 contains pairs (2.015, 2.025), (2.035, 2.045), etc.

The collection of spectral features with cumulative probability less than 0.005 shown in Table 4.1 illustrates the prominence of several features in multiple spectra. It is necessary to estimate the number of features one would expect in the table for a certain significance if one considers every bin in all 12 binnings of a particular spectrum within the selection region as an independent test for an emission line. It has been shown empirically using Monte-Carlo simulations that for binned random noise, subsequent binnings of the same data by a factor of 2 are approximately independent of each other (Butler et al. 2003). There were 1500 bins in the selection region of the spectrum with finest binning, 750 in the rebinned spectrum of that, 375 in the next, etc., for 6 binnings each of the spectra of the entire jet, Knot A, and Knot B. This totals 2954 independent tests each for a feature of Knot A or Knot B. There are 8 features in the spectrum of the entire jet in Table 4.1 with cumulative probabilities less than .0014, and one expects .0014 * 2954= 4.136 features with this probability or less on average. We now assess the significance of finding 8 or more features when the expected number of 4.136. This is another Poisson process with k=8,9,10... and λ=4.136. This gives a cumulative probability of about 0.060. Therefore, it is likely at least one of these events is not random with confidence of 94%. This is a 2 sigma deviation from random noise if transforming to Gaussian confidence intervals.

It is important to note that the candidate features which appear in spectrum of the entire jet generally do not also appear in the spectrum of knot A. The cause for this is as yet unknown but there is an ongoing investigation to try to determine if it is due to different Doppler shifts for the X-rays from the two primary knots. This is discussed further in Chapter 5.

In Chapter 5 I consider physical sources of these possible narrow emission lines and what their identification can tell us about the jet.

Table 4.1: Selected Candidates for Narrow Emission Lines

λ $(\overset{\circ}{A})$	S	$\Delta\lambda$ $(\overset{\circ}{A})$	Initial Pairs Set	Selection Region (Knot A, B, or Full)
2.145	0.00132525	.01	1 + 2	Full
	0.00202477	.01	1 + 2	A
(2.140)	0.000132343	.02	2	Full
	0.0008479	.02	2	A
(2.130)	0.00235807	.04	2	Full
3.885	0.000659066	.01	1 + 2	Full
4.03	0.00304	.02	1	A
4.175	0.00241983	.01	1 + 2	B
4.275	0.00201054	.01	1 + 2	B
(4.280)	0.00100555	.02	2	Full
	0.00253966	.02	2	B
4.985	0.000612884	.01	1 + 2	A
(4.95)	0.001107	.02	2	A
5.870	0.000882901	.02	1	Full
	0.0008278	.02	1	A
6.160	0.000555123	.02	2	Full
	0.000182983	.08	1	B
	0.000898226	.02	2	B
	0.00294182	.08	1	Full
(6.19)	0.00219795	.16	2	B
(6.200)	0.000922494	.16	1	B
(6.270)	0.000770190	.32	2	B
(6.280)	0.00183102	.32	1	B
6.765	0.00143261	.01	1 + 2	A
6.815	0.00225705	.01	1 + 2	B
(6.810)	0.000788610	.02	1	B
7.925	0.000717927	.01	1 + 2	A
(7.93)	0.000989	.02	1	A
10.405	0.00287947	.01	1 + 2	B
12.335	0.00106038	.01	1 + 2	B
(12.330)	0.00105922	.02	1	B
(12.340)	0.00235510	.02	2	B
13.65	0.00254	.04	2	A
15.18	0.00278172	.02	2	A
	0.001412	.04	1	A
(15.20)	0.0012795	.08	1	A
16.285	0.000663424	.01	1 + 2	Full
(16.300)	0.00133998	.04	1	Full
16.855	0.00272909	.01	1 + 2	Full
16.965	0.00301924	.01	1 + 2	B

45

Chapter 5

Calculation of Jet Speed

5.1   Identification of Emission Line Candidates

There is still very little known about the physics governing quasar jets and it would be useful to be able to compare simulations and models of jets of AGN to constrained data from observations. In this chapter I consider possible X-ray emission lines which fit the observed spectral lines described in Table 4.1. Once the lines are identified their relative strengths are compared to x-ray emission models of a hot plasma, the speed of the plasma is inferred from the relativistic Doppler shift, and the densities of the identified components of the plasma are calculated.

5.2   Line Identification and Plasma Temperature

In order to identify possible X-ray emission lines that would match the observed narrow line candidates found in Chapter 4, we compared these candidates to known X-ray emission lines. Using the listing of lines calculated by the Mewe plasma code, provided by Alex Brown of the U. Colorado, which includes all known strong emission lines between 1.29 and 296.11 Å a database list was formed in IDL of all lines with values of α less than 1.01 where α represents the line emissivity ϵ through

$$\epsilon = 10^{-(\alpha+23.00)} \text{ ergs cm}^3 \text{ s}^{-1} \tag{5.1}$$

Thus, smaller values of α represent strong emission lines. I wrote a procedure which takes a list of emission line candidates as input (with wavelengths as measured by the HETG) and finds the ratio of the first of these wavelengths to the wavelength of each strong emission line included in the database. The ratio, δ, contains the information about the total Doppler shift that would have occurred if the matching of this observed line to the emission line is correct. Using this ratio, the wavelength in the rest frame of emission is found for the other input line candidates, and these are compared to other lines in the database. We are allowed to do this because this ratio is the same for all lines in the spectrum assuming they are emitted by plasma moving at a single velocity. Assuming a match between the first candidate and a certain database line, other database lines were selected if they were within ± 0.05 Å of another input candidate. The output of the procedure contained the information about how many of the input candidates could be matched with lines beyond the first, and what the ratio was for that set of matches. Assuming a correct match, this ratio can be used, as described in Section 5.3, to calculate the velocity of the plasma in the jet knots.

My input list of candidates was chosen from Table 4.1 based on their significances: 6.16 Åwas used as the important first candidate, then 2.14, 3.885, 4.28, 5.87, 6.81, and 16.285 Å. The procedure output for this list was ten values of δ – nine cases in which two lines were matched and one in which there were three.

In order to narrow down our choices an important assumption was made: the temperature of the X-ray emitting plasma in the knots was of roughly uniform temperature, with an allowance of $\pm .1$ in the log of the temperature. Several values of the emissivity are given in the table from the Mewe plasma code for each line showing their dependence on plasma temperature. Using the ratio of the strengths of observed lines one can thus infer the temperature of the X-ray emitting plasma. We also know that for a given δ, the matching emission lines must be correct to within 0.01 Å the accuracy of the wavelengths of the table. These values are especially well known for strong emission lines. Another test is whether or not the given constant shift matches other strong lines in the table which have the same temperature and

Table 5.1: X-ray Emission Line Matches

Candidate λ	Matching Species	Species λ	Temp. (log K)	α
5.87	Fe XVIII	14.28	6.8	1.49
6.16	Fe XVII	15.01	6.8	.86
6.27	Fe XVII	15.26	6.8	1.36

atoms with candidates in the jet knot spectra not included in the input candidate list.

Using these tests the most reasonable selection of matching candidates is summarized in Table 5.1. The Fe XVII line at an observed 6.27 Å is considered because there is a drop in cumulative probability for the bin including 6.16 Å when going from 0.16 to 0.32 Å binnings, thus possibly including a weak feature at 6.27 Å .

The constant spectral shift factor for these two matches is 2.43669.

5.3 Doppler Shift

There are two Doppler shifts which affect emission lines from moving plasma along the jet of 3C 273. The first comes from the redshift of the quasar itself and the second from the motion of the knots in the rest frame of the quasar.

The Doppler shift of 3C 273 comes from the cosmological redshift due to the expansion of the universe. z = .158 in this case where

$$1 + z = \frac{a(t_o)}{a(t_e)} \tag{5.2}$$

$a(t)$ is the cosmological scale factor as a function of time, and t_o and t_e are the time at which a photon is observed and emitted, respectively.[1]

We also have to taken into account the relativistic Doppler shift of X-rays emitted by the jet knots, which is dependent on the direction of motion with respect to the line of sight. The equation giving the Doppler shift for motion with unitless velocity

---

[1]This calculation is under a flat cosmology with Ω_m=0.3 and H_o=70km /s / Mpc, which leads to a scale of 2.7 kpc per arcsec at redshift 0.158. (Jester et al. 2006)

β=v/c, where c is the speed of light and v is the velocity in the same units, at an angle θ_o off of the line of sight from the knot to the observer, is

$$\lambda_e = \lambda_o \frac{\sqrt{1 - \beta^2}}{1 - \beta \cos(\theta_o)} \qquad (5.3)$$

where λ_o is the wavelength of the light measured in the observer's reference frame and λ_e is the wavelength emitted by the source, in this case the plasma of the jet knots.

We obtained the value of the spectral shift ratio

$$\delta = \frac{\sqrt{1 - \beta^2}}{1 - \beta \cos(\theta_o)}(1 + z) \qquad (5.4)$$

through our matching algorithm described in Section 5.2, but we have two free parameters to constrain, β and θ_o. While the angle of the jet is not well known at this time, we take the value of 2.5 degrees as estimated by Marshall et. al. (2005). This allows us to estimated the bulk velocity of the jet knots to be $\beta \approx 0.78$. Note, however, that there are two solutions since the equation is quadratic in β. This comes from the fact that the angle to the line of sight is non-zero. The second solution, $\sim$0.999996, corresponds to a Lorentz factor of $\sim$350. This solution is unlikely since it is not in agreement with measures by Davis et al. (1991) of jet flow near the core through observation of superluminal motion, or measures of bulk velocity in the jet assuming X-ray emission through inverse Compton scattering of photons from the Cosmic Microwave Background (CMB) (Marshall et al. 2005).

5.4 Density

With our selection of spectral emission lines from the knots we have all parameters required to calculated the electron density using our measure of Fe XVIII and Fe XVII line emission in the jet knots. For this calculation I take the values of line flux from the entire jet since these lines are not both clearly resolved in the spectrum of Knot A, mostly likely due to small photon counts in this source selection region.

We start with the equation for the luminosity of a specific X-ray emission line signified by 'x'

$$L_x = \int j_x(\epsilon, T) n_e^2 \, dV.$$ (5.5)

where j_x is the emissivity of species x, n_e is the electron density in the plasma, and the integral is over the volume of the plasma emitting the emission line x. This integral over the entire volume gives the luminosity, which has units of [ergs/s]. The emissivity has units [erg cm^3 / s] as mentioned before, and the density is in particles per cubic centimeter.

If we assume uniform density distribution, we can simplify 5.5 to

$$L_x = j_x n_e^2 V$$ (5.6)

where V is the approximated volume of the jet knots.

A second equation for luminosity is that calculated from the observed photon flux:

$$L_x = f_x E_x 4\pi D^2$$ (5.7)

where f_x [photons / cm^2 / s] is the line flux of emission line x, E_x [erg / photon] is the energy of the line, and D [cm] is the distance to the source from the observer. Line flux is given by

$$f_x = \frac{C_x}{A_{eff}\tau_{exp}}$$ (5.8)

where C_x [photons] is the number of photon counts in the $\Delta\lambda$ for line x, and A_{eff} [cm^2] is the effective area at λ_x.

We can set these two equations for luminosity equal to each other and solve for electron density.

$$\frac{C_x}{A_{eff}\tau_{exp}} E_x 4\pi \mathrm{D}^2 = j_x n_e^2 V$$ (5.9)

$$n_e = \sqrt{\frac{C_x E_x 4\pi D^2}{A_{eff}\tau_{exp} j_x V}}$$ (5.10)

I take a distance of D = 749 Mpc as in Uchiyama et. al (2006), $E_x = \mathrm{hc}/\lambda_x$

51

with $\lambda_x = 15.01$ Å an exposure time of 234.52 ks, emissivity exponent $\alpha = 0.86$ at $10^{6.8}$ K, total average number of counts in $\Delta\lambda_x = 0.02$ Å above the background as $C_x = 15.6 \pm 5.7$, and an estimate of the total volume of the X-ray emitting plasma in the jet of V. I estimate V by approximating Knots A and B to be spherical with diameters in the line of sight of 2 arcsec each, and the remainder a cylindrical column with diameter 1arcsec and length 5 arcsec with an inclination out of the line of sight of 2.5° as before. Thus, $V \approx 2.97 \times 10^{68}$ cm^3. $E_x = 3.22 \times 10^{-9}$ ergs. $A_{eff} = 18.879$ cm^2. With these values we get an electron density of $n_e = 0.043\pm^{.007}_{.009}$ cm^{-3}.

Chapter 6

Concluding Remarks

Using data from 8 observations of 3C 273 and its jet using the HETGS on the Chandra X-ray Observatory, we were able to study the high-resolution X-ray spectrum of the jet knots A, B, and the entire jet. Using these spectra we searched for narrow emission line candidates in wavelength binnings of 0.01, 0.02, 0.04, 0.08, 0.16, and 0.32 Åbinnings.

Based on significance values calculated for the observed photon counts in each bin of the spectrum of the entire jet, we selected three possible emission line candidates and attempted to match these lines with known highly emissive X-ray emission lines thereby inferring the temperature of the X-ray emitting plasma making up the material of the jet knots, the bulk velocity of the knots, and the electron density in the jet.

Bibliography

[1] Bennett, A.S., 1961, Mem. of Roy. Astr. Soc., 68, 163.

[2] Born, M. and Wolf, E. *Priciples of Optics: electromagnetic Theory of Propagation, Interference, and diffraction of Light, 6th ed.* (New York: Pergamon Press 1980), pp. 55-67.

[3] Butler, N., et al. 2003a, ApJ, 597.

[4] Canizares, C.R. et al. *The Chandra High Energy Transmission Grating: Design, Fabrication, Ground Calibration, and Five Years in Flight* 2005.

[5] Carroll, B.W., Ostlie, D.A., *An Introduction to Modern Astrophysics.* 2nd Ed. (Pearson: Addison-Wesley 2007.)

[6] CXC, CPS, C IPI Teams, *The Chandra Proposer's Observatory Guide*

[7] Davis, R.J., Muxlow, T.W.B., & Unwin, S.C. 1991, Nature, pp. 254-374.

[8] Edge, D.O. et al. 1959, Mon. Not. R. Astron. Soc., 68, 11, 360.

[9] Gelbord, J.M. et al. *Continuing A Chandra Survey of Quasar Radio Jets.* X-ray and Radio Connections (L.O. Sjouverman & K.K. Dyer, editors. 2005)

[10] Georganopoulos, M. et al. *Quasar X-ray jets: Gamma-ray diagnostics of the synchrotron and inverse-compton hypotheses, the case of 3C 273* 2006. Astrophysical Journal Letters, 653, L5.

[11] Hazard, C., Mackey, M.B., Shimmins, A.J., 1963, Nature, Vol. 197, pp. 1037.

[12] Jester, S. et al. 2006, ApJ.

[13] Woltjer, L. 1959. Ap. J. 130, pp. 38.

[14] Kundt, W. (Ed.), *Jets from Stars and Galactic Nuclei.* Proceedings, Bad Honnef, Germany 1995. (Springer 1996)

[15] Marshall, H.L. et al. 2001, ApJ, 549, L167.

[16] Marshall, H.L. et al. *X-ray Emission From the 3C 273 Jet* 2005.

[17] Marshall, H.L. et al. *A Chandra Survey of Quasar Jets: First Results.* 2005. ApJS 156, 13-33.

[18] Mewe, R. 1992. In Proc. Workshop of UK SERC's Collaborative computation Project No 7 (CCP7) on The physics of chromospheres, coronae and winds, eds. C.S. Jeffery and R.E.M. Griffin. (Cambridge University Printing Service). p. 33.

[19] Peterson, B.M. *An Introduction to Active Galactic Nuclei.* (Cambridge University Press, 2003.)

[20] Roser, H.-J., et al. 2000, *The jet of 3C 273 observed with ROSAT HRI*, A&A, 360, 99-106.

[21] Schmidt, M. 1963, Nature, Vol. 197, 1040.

[22] Uchiyama, Y., et al. 2006, ApJ, 648, 910